Earth and Planetary Science Letters ••• (••••) •••–•••

Contents lists available at SciVerse ScienceDirect

Earth and Planetary Science Letters

www.elsevier.com/locate/epsl

Aseismic deformation across the Hilina fault system, Hawaii, revealed by wavelet analysis of InSAR and GPS time series

M. Shirzaei [a,b,*], R. Bürgmann [a], J. Foster [c], T.R. Walter [d], B.A. Brooks [c]

[a] Department of Earth and Planetary Science, University of California, Berkeley, CA, USA
[b] School of Earth and Space Exploration, Arizona State University, Tempe, AZ, USA
[c] Hawaii Institute of Geophysics and Planetology, 1680 East-West Rd. Honolulu, HI 96822, USA
[d] Section 2.1, Dept. Physics of the Earth, GFZ German Research Center for Geosciences, Telegrafenberg, D-14473 Potsdam, Germany

ARTICLE INFO

Article history:
Received 2 December 2012
Received in revised form 7 June 2013
Accepted 8 June 2013
Available online xxxx
Editor: P. Shearer

Keywords:
InSAR
wavelet analysis
cluster analysis
landslide
Hawaii

ABSTRACT

The Hilina Fault System (HFS) is located on the south flank of Kilauea volcano and is thought to represent the surface expression of an unstable edifice sector that is active during seismic events such as the 1975 Kalapana earthquake. Despite its potential for hazardous landsliding and associated tsunamis, no fault activity has yet been detected by means of modern geodetic methods, since the 1975 earthquake. We present evidence from individual SAR interferograms, as well as cluster analysis and wavelet analysis of GPS and InSAR time series, which suggest an inferred differential motion at HFS. To investigate the effect of atmospheric delay on the observed differential motion, we implement a statistical approach using wavelet transforms. We jointly analyze InSAR and continuous GPS deformation data from 2003 to 2010, to estimate the likelihood that the subtle time-dependent deformation signal about the HFS scarps is not associated with the atmospheric delay. This integrated analysis reveals localized deformation components in the InSAR deformation time series that are superimposed on the coherent motion of Kilauea's south flank. The statistical test suggests that at 95% confidence level, the identified differential deformation at HFS is not due to atmospheric artifacts. Since no significant shallow seismicity is observed over the study period, we suggest that this deformation occurred aseismically.

1. Introduction

The recurrence intervals of large earthquakes ($M > 7$) that are accompanied by secondary failure along the Hilina Fault System (HFS) is estimated to be ~80–260 years (Cannon and Bürgmann, 2001). Slip along the HFS is documented during the 1975 and 1868 seismic events, which ruptured a deep decollement fault below Kilauea volcano's south flank (e.g. Ando, 1979; Cannon and Bürgmann, 2001; Owen and Burgmann, 2006) and were accompanied by tsunami waves of up to 15 m height (Goff et al., 2006; Ma et al., 1999).

The down-dip geometry of the HFS is not well constrained, possibly being either a shallow slump structure (<3 km) that is active during major earthquakes (Cannon and Bürgmann, 2001; Morgan et al., 2003), or representing the surface trace of a major and deep structure connected to the basal decollement at ~9 km depth (Parfitt and Peacock, 2001). A lack of shallow seismicity (<5 km) beneath the HFS (see Fig. S1) suggests that the HFS is likely to be locked or displacing aseismically. However, difficulties with studying subtle localized deformation along the HFS come from: (1) the fact that the whole Kilauea south flank moves continuously seaward, and (2) the sparseness of existing GPS networks with respect to the HFS structural segmentation. Nonetheless, because of the intermittent occurrence of destructive earthquakes and associated tsunamis, characterizing the internal deformation of the southern Kilauea flank as well as the HFS is of great importance.

In this paper we investigate large datasets of both InSAR (interferometric synthetic aperture radar) and GPS (global positioning system) time series measuring seven years of deformation across Kilauea's south flank. Evidence that suggests differential movement across several stands of the HFS includes sharp fringe discontinuities observed in individual wrapped interferograms that correlate with the surface expression of the HFS scraps. Furthermore, cluster analysis of the InSAR deformation time series identifies classes of coherently moving points that coincide with blocks bounded by the HFS. Next, to test the hypothesis that the signal observed is not due to atmospheric delay, we jointly analyze the InSAR and GPS datasets using a new wavelet based statistical frame work. Wavelet transforms enable decomposing the deformation time series into their building blocks and allow identification of non-stationary components, such as transient motions and atmospheric delay, as well as steady ones.

* Corresponding author at: School of Earth and Space Exploration, Arizona State University, Tempe, AZ, USA.
E-mail address: shirzaei@asu.edu (M. Shirzaei).

0012-821X/$ – see front matter
http://dx.doi.org/10.1016/j.epsl.2013.06.011

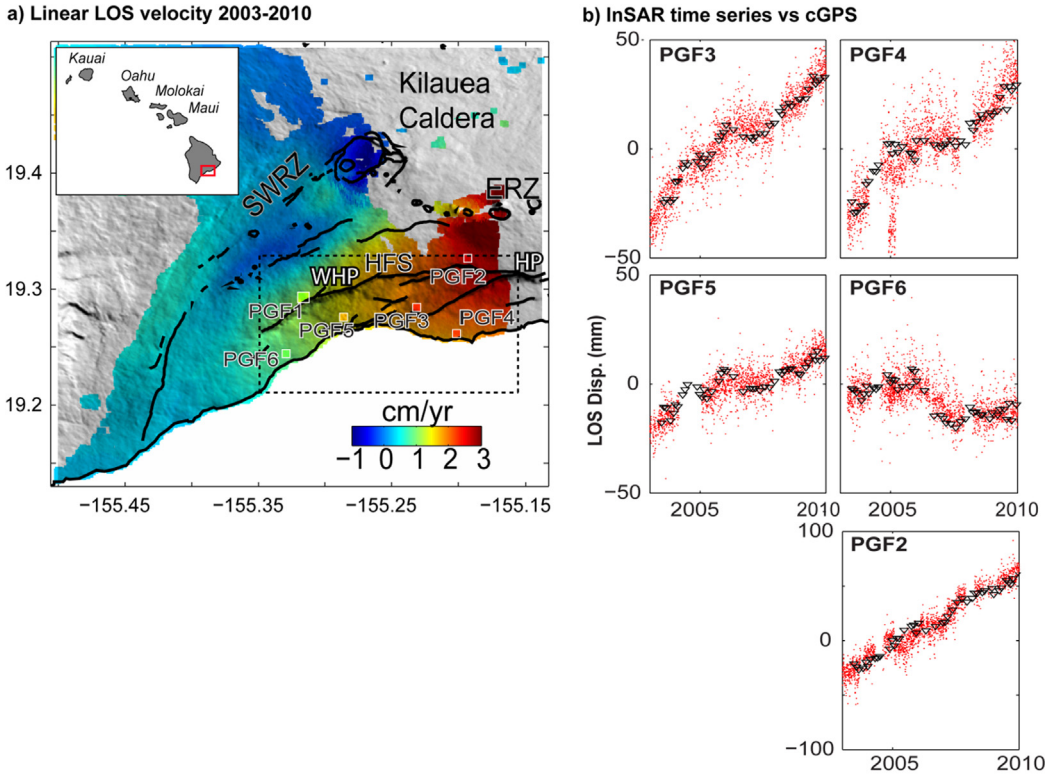

Fig. 1. (a) The linear velocity field in the line of sight of the descending-orbit Envisat satellite (track 200) over the Kilauea south flank from 2003 till 2010. Area of the study, Hilina Fault System (HFS), is outlined by dashed box. Location of GPS stations used is marked by their names next to filled squares colored by the mean rate of motion in the LOS direction. Station PGF1 is the reference for both GPS and InSAR datasets. WHP = western Hilina Pali, HP = Holei Pali. (b) The time series of relative GPS and InSAR displacements in the LOS direction at the location of the GPS stations marked with filled squares.

Through this study we show that while the whole Kilauea south flank moves seaward, blocks along the HFS undergo transient episodes of aseismic motion. This result has important implications for tsunami hazards in the Pacific Ocean and for other oceanic islands. Although large-scale flank failures are rare (the most recent occurred about one hundred thousand years ago, e.g. Moore et al., 1994), Hawaiian landslides are among the largest known on Earth and to date more than fifteen giant landslide deposits have been identified surrounding the Hawaiian Islands (McMurtry et al., 2004; Moore et al., 1994). Tsunamis resulting from these catastrophic failures could generate waves of up to 300 m (McMurtry et al., 2004). Therefore, characterizing the dynamics of unstable flank blocks is of great importance to forecast future hazards.

2. Deformation data and validation

To study the spatiotemporal deformation field over the HFS on Kilauea's south flank, we used three independent deformation datasets, including two separate InSAR time series and continuous GPS observations, which we briefly describe in the following.

2.1. InSAR deformation field

To obtain a dense map of the spatiotemporal deformation field over Kilauea's south flank, we analyze two SAR datasets of 44 and 39 images acquired from 2003 to 2010 in the descending orbit mode (azimuth = 188° and incidence angle = 23°) of the Envisat radar satellite along, tracks 200 and 429, respectively (Fig. S2). The data catalogue is almost complete, with an average temporal sampling rate of ∼58 and ∼65 days. Using this data, we generate two sets of ∼520 and ∼430 interferograms with spatial and temporal baselines smaller than 450 m and 4 years, respectively.

Figs. 2 and S3 show examples of individual wrapped interferograms. We note that the fringe patterns exhibit sharp offsets across several of the HFS scarps, in particular across the western Hilina Pali and Holei Pali. Fig. S3 shows the corresponding estimates of topography-correlated atmospheric delay, which is used to correct the interferograms following Shirzaei and Bürgmann (2012). The estimates of the atmospheric error are of large amplitude and highly variable and also tend to be influenced by the large topographic scarps of the HFS (Figs. S3, S4).

To generate spatiotemporal maps of the deformation field we employ the WabInSAR (Wavelet based InSAR) approach, following Shirzaei (2013). Using the WabInSAR approach, the topographic phase has been simulated and removed using precise satellite orbits and a reference Digital Elevation Model (DEM) (Franceschetti and Lanari, 1999). To obtain the unambiguous differential phase data in each interferogram, an iterative phase unwrapping followed by a low pass filter is implemented. Phase unwrapping is applied to those pixels containing a lower level of decorrelation noise (Costantini and Rosen, 1999). To identify less noisy pixels, we use a statistical scheme to examine interferometric phase noise (Shirzaei, 2013). The unwrapped interferograms are corrected for the orbital error and the topography correlated component of the atmospheric delay using methods proposed by Shirzaei and Walter (2011) and Shirzaei and Bürgmann (2012). These methods use wavelet multiresolution analysis and robust regression to distinguish between various components of the interferometric phase and extract environmental artifacts. The unwrapped and corrected interferograms are inverted using a re-weighted least squares approach (Shirzaei, 2013) to generate a time series of the deformation field. To reduce the temporal component of the atmospheric delay, we apply a low pass temporal filter based on continuous wavelet transforms (Shirzaei, 2013).

Figs. 1a and S2 show the line-of-sight (LOS) velocity field for track 200 and 429, respectively. The results reveal deformation that affects most of the south flank. However, no localized fault-

Please cite this article in press as: M. Shirzaei et al., Aseismic deformation across the Hilina fault system, Hawaii, revealed by wavelet analysis of InSAR and GPS time series, Earth Planet. Sci. Lett. (2013), http://dx.doi.org/10.1016/j.epsl.2013.06.011

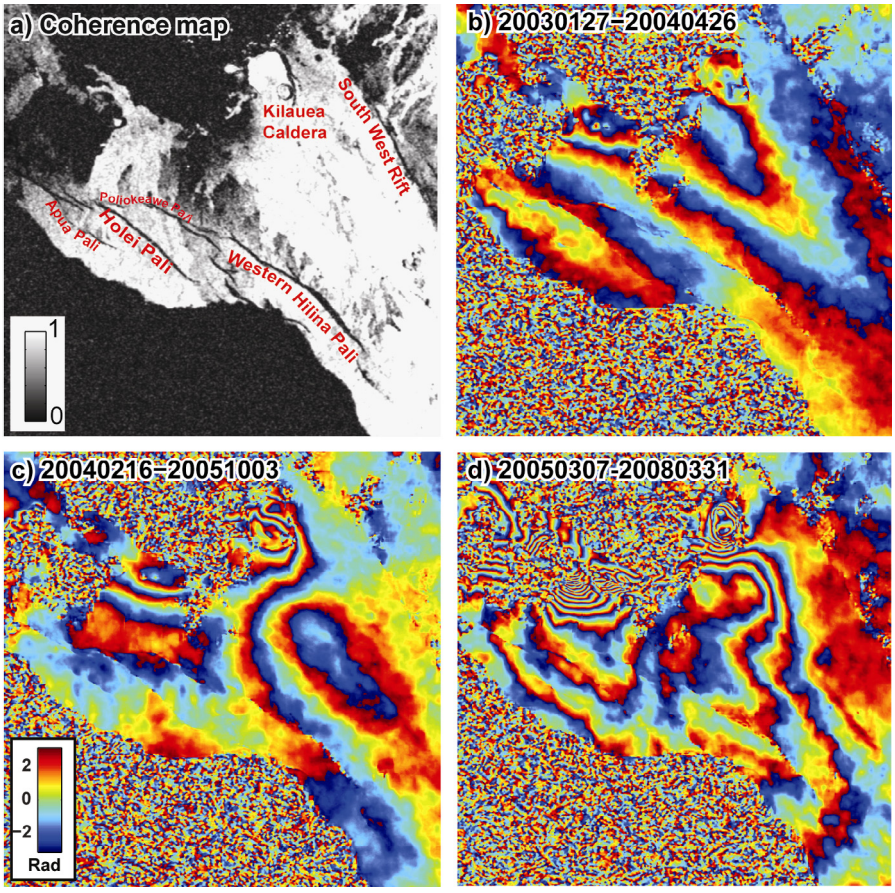

Fig. 2. Evidence of differential motion across the HFS blocks from individual interferograms, (a) example of interferometric coherence map highlighting major volcanic and tectonic features. (b–d) three examples of independent interferograms showing phase discontinuities across several of the HFS fault traces. Note that these wrapped interferograms are plotted in range-azimuth coordinates leading to the flipped orientation.

ing is visible at the HFS in the LOS velocity data. As we will show below, subtle local deformations may be hidden due to the complexity of the time-dependent deformation field that overlays the signals.

2.2. GPS data set

The GPS data are obtained from the University of Hawaii continuous network on Kilauea (Brooks et al., 2006). To estimate the displacement time series and long-term velocities, daily cGPS measurements of available Hawaii stations and IGS sites around the Pacific are processed using the GAMIT and GLOBK software (Herring, 2005; King and Bock, 2005) and precise orbits provided by the Scripps Orbit and Permanent Array Centre (SOPAC) (http://sopac.ucsd.edu). See Brooks et al. (2006) for further details on the GPS analysis.

2.3. InSAR time series validation

The InSAR deformation time series are compared with the GPS data. To this end we projected the three components of displacement at the GPS stations into the LOS direction of the Envisat satellite and compare with the average range change for pixels within a circle of 200 m radius around each station. As seen in Figs. 1b–1f, the InSAR data agree well with the GPS data obtained at five stations relative to the reference site PGF1. This good agreement illustrates that the applied algorithms for time series generation and filtering are effective and able to correct general contributions of the atmospheric delay.

3. Evidence of differential deformation across the HFS

In this section we summarize the evidence indicating apparent differential motion across the HFS. The first evidence is obtained through careful assessment of the individual generated interferograms over the HFS. Fig. 2a shows an interferometric coherence map highlighting the major fault traces of the HFS. Figs. 2b–2d present three independent interferograms spanning almost 1, 2 and 3 years of deformation on Kilauea's south flank. Additional examples are shown in Fig. S3. In all of them, there are clear discontinuities in the fringe pattern, which coincide with the major traces of the HFS. These breaks of the continuous fringe patterns suggest shallow and localized deformation at HFS. We note that the sign of the apparent phase discontinuity is variable, suggesting that both normal and reverse offsets occur (Fig. S5).

The second evidence comes from cluster analysis of the InSAR deformation time series generated and validated in Section 2. The cluster analysis is a data mining tool for bundling together similar objects to produce a classification, see e.g. Everitt (2011). The similarity between members of a class is often quantified using a metric distance. Given the effectiveness and easily applicability of the clustering approach to high-dimensional and large scale data sets, it has been widely used in various disciplines, e.g., Houser et al. (2008), Lekic et al. (2012), Luhr et al. (2010), Simpson et al. (2012). In here, to classify the InSAR deformation time series, we use the MATLAB command '*clusterdata*'. This algorithm provides a flexible approach to apply various metric distances to obtain a classification of the InSAR time series. Following Simpson et al. (2012), we adopted an Euclidean (or L_2-norm) distance metric to charac-

Please cite this article in press as: M. Shirzaei et al., Aseismic deformation across the Hilina fault system, Hawaii, revealed by wavelet analysis of InSAR and GPS time series, Earth Planet. Sci. Lett. (2013), http://dx.doi.org/10.1016/j.epsl.2013.06.011

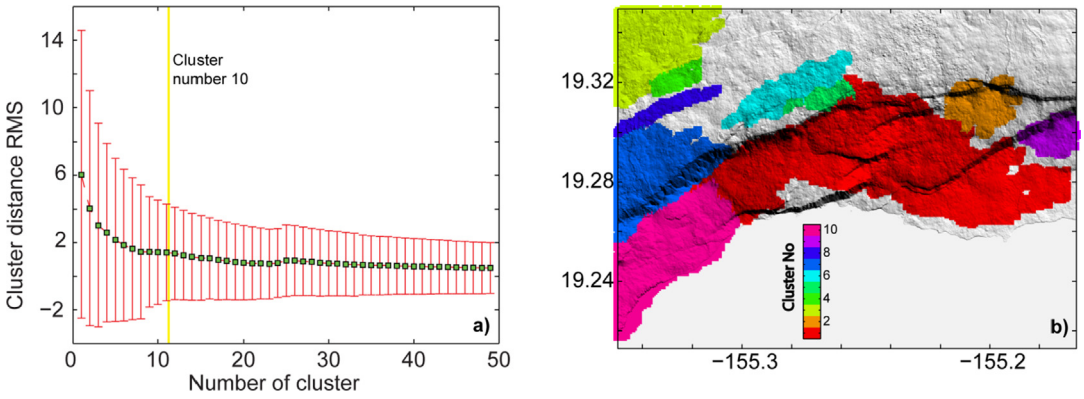

Fig. 3. Evidence of differential motion across the HFS blocks from cluster analysis of the InSAR deformation time series. (a) Cluster distance root mean square versus number of clusters, used to identify the optimum number of clusters. (b) Spatial distribution of the identified clusters. The cluster analysis is applied to the deformation time series of each elite pixel and the measure of the similarity is the Euclidean distance between pairs of time series. To reduce the effects of outliers, we only consider classes with 100 or more members.

terize the similarity of the deformation time series of track 200. The cluster analysis is applied to the time series of the deformation at each pixel and thus, only the temporal information is used for classification. Also, to assure significance of each class and to reduce the effect of outliers, we only consider classes with 100 or more members. Prior to applying the cluster analysis, one needs to decide about the number of the classes that the method is reliably able to identify. Simpson et al. (2012), following Tibshirani et al. (2001), suggest that the cluster distance RMS drops rapidly down to the optimum cluster number and afterward declines more gradually. The curve showing the cluster distance RMS versus number of clusters is presented in Fig. 3a. The RMS drops rapidly until cluster number 10, which we chose as the optimum number of clusters. Fig. 3b shows the spatial distribution of the clusters. Note that several of the classes are bounded by the major traces of the HFS, which suggests that these blocks undergo similar deformation histories that distinct from adjacent blocks.

So far, we have presented two independent lines of evidence of localized differential motion across the HFS. In the next section and using wavelet analysis of the InSAR and GPS data in a statistical framework, we argue that the observed signal is significant and is not due to atmospheric delay.

4. Statistical wavelet analysis of the deformation time series

Given the advantage of wavelet for multiscale analysis, recently there has been a growth in application of wavelets, in particular for SAR analysis, which includes; precise orbital error correction (Shirzaei and Walter, 2011), topography correlated atmospheric delay reduction (Shirzaei and Bürgmann, 2012), differential interferogram inversion and time series generation (Hetland et al., 2012) and a new approach for multitemporal InSAR analysis including pixel selection, atmospheric and tropospheric error reduction, phase unwrapping and time series generation proposed by Shirzaei (2013). Here and to further explore the deformation data over the HFS (area marked by dashed-line box in Fig. 1a and estimate the statistical significance of the components of the deformation field correlating with the HFS blocks, we analyze the InSAR and GPS time series using continuous wavelet transforms (CWT).

The CWT of a time series $X(n)=\{x_n\}_{n=1..N}$ (here, the InSAR and GPS deformation time series) with a time step δt can be defined via convolution with a scaled and normalized wavelet function (ψ_0) as follows (Torrence and Compo, 1998):

$$W(a,n)=\psi^T(n,a)*X(n)$$

$$\psi(n,a)=\left(\frac{\delta t}{a}\right)^{1/2}\psi_0\left(\frac{n\delta t}{a}\right) \tag{1}$$

where a is a scaling parameter, $(^T)$ is the complex conjugate, and $(*)$ is the convolution operator. CWT can be evaluated using the convolution theorem in the Fourier domain (Torrence and Compo, 1998). We also define the global wavelet spectrum (G) at scale a as:

$$G(a)=\frac{1}{N}\sum_{n=1}^{N}\left(W(a,n)\right)^2 \tag{2}$$

Using linear algebra, Eq. (1) can be re-written in the following form:

$$W(a,n)=\Psi(n,a)X(n) \tag{3}$$

where Ψ is a $n\times n$ circulant matrix, ψ is the first row of Ψ and each row vector is rotated by one element forward relative to the preceding one. Given the linearity of Eq. (3), both the wavelet coefficients and the time series have a similar probability density function.

To obtain the variance–covariance matrix of the wavelet coefficients, we further explore Eq. (3). Given Q_{xx} is the variance–covariance matrix of a time series $X(n)=\{x_n\}_{n=1..N}$, the variance–covariance matrix ($Q_{W_aW_a}$) of the wavelet coefficients at scale a is obtained as:

$$Q_{W_aW_a}=E\left[W(n,a)-E\left[W(n,a)\right]\right]E\left[W(n,a)-E\left[W(n,a)\right]\right]^T \tag{4}$$

where E is the statistical expectation. Substituting Eq. (3) in (4) yields:

$$Q_{W_aW_a}=\Psi(n,a)Q_{xx}\Psi(n,a)^T \tag{5}$$

Eq. (4) presents the variance–covariance matrix of the wavelet coefficients that is obtained based on a variance–covariance matrix of the observed time series.

Using the math detailed above, we are able to calculate the wavelet transform of a time series and the associated variance–covariance matrix, which allows establishing a statistical framework to estimate the significance of the agreement of InSAR versus GPS.

Assume two time series of $X(n)=\{x_n\}_{n=1..N}$ and $Y(n)=\{y_n\}_{n=1..N}$ are two independent measurements of a quantity (in here: the time series of InSAR and GPS deformation at the location of each GPS station). The corresponding coefficients of the wavelet

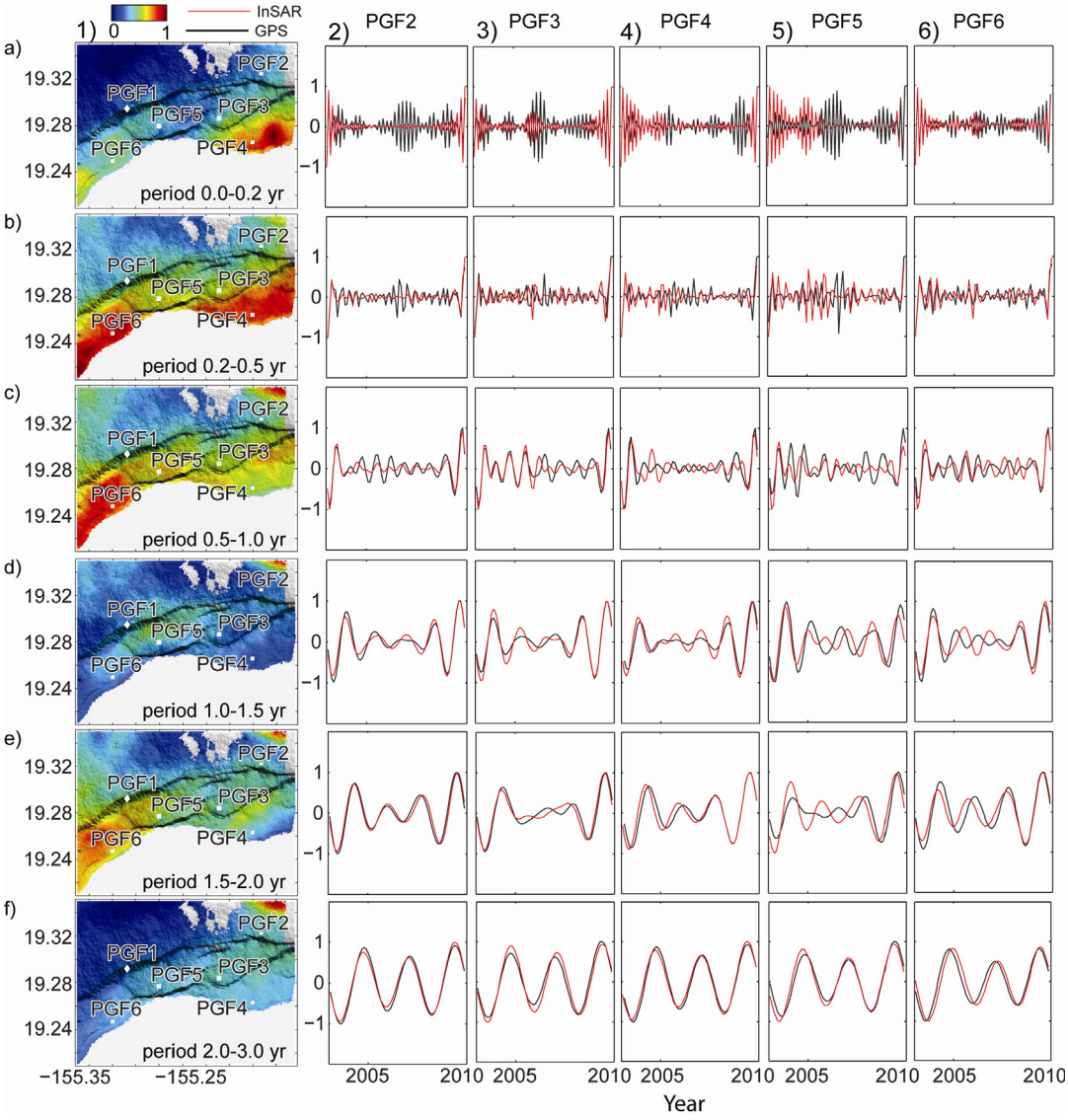

Fig. 4. The results of wavelet analysis of GPS and InSAR time series. This figure has 36 panels including 6 rows and 6 columns. We label the rows of this figure by letters from 'a' through 'f' and columns by numbers from '1' to '6', for instance b4 refers to the panel located at row 'b' (period range 0.2–0.5 years) and column '4' (PGF4). Panels a1–f1 present the global wavelet spectrum for different frequency classes obtained by wavelet analysis of InSAR time series from track 200. Panels a2–f6 shows the comparison of the wavelet coefficients for InSAR (blue) and GPS (black) time series. Note that the colorbar and y-axes values represent dimension-less quantities related to wavelet coefficients. Thus the larger the value the more significant is its impact on the deformation observed with InSAR and GPS. See also Fig. S4 for the associated errorbar of the InSAR and GPS wavelet coefficients.

transform at scale a and sample n are ω_x and ω_y with associated variance of σ_x and σ_y, respectively. Therefore, the following statistic for the wavelet-coefficient-difference $(\omega_x - \omega_y)$ holds:

$$\frac{\omega_x - \omega_y}{\sqrt{\sigma_x^2 + \sigma_y^2}} \sim N(0,1) \tag{6}$$

where $N(0,1)$ is the normal distribution function and the statistical expectation $E(\omega_x - \omega_y) = 0$. Accordingly, a $(1-\alpha)\%$ confidence interval for the wavelet-coefficient-difference can be presented as following:

$$-\sqrt{\sigma_x^2 + \sigma_y^2} N_{1-\alpha/2} < \omega_x - \omega_y < \sqrt{\sigma_x^2 + \sigma_y^2} N_{1-\alpha/2} \tag{7}$$

The failure of this test means that $E(\omega_x - \omega_y) \neq 0$, indicating that the components of the InSAR time series are contaminated by systematic errors, such as atmospheric delay. Thus the statistical framework presented above allows for testing the hypothesis the observed signal at HFS is not due only to observation artefacts.

4.1. Wavelet classification of the InSAR and GPS time series

In this section we present the result of wavelet analysis of the time series obtained by GPS and InSAR over the HFS, using Eqs. (1)–(5). The results of the analysis for track 200 and 429 are presented in Figs. 4, S6 and S7, respectively. To reduce the amount of data, we focus on the following frequency classes, including periods 0.0–0.2, 0.2–0.5, 0.5–1.0, 1.0–1.5, 1.5–2.0 and 2.0–3.0 years. Figs. 4a1–4f1 present the spatiotemporal distribution of the normalized global wavelet spectrum (Eq. (2)) for these six frequency classes obtained by analysis of the InSAR time series. These values are normalized, thus dimensionless and the red color is equivalent to a large quantity of LOS displacement at the given period. Figs. 4a2–4f6 show the comparison of the wavelet coefficients for the InSAR and GPS time series (Eq. (1)). Fig. S6 shows the same information as Fig. 4, but also the associated 2σ uncertainties for the InSAR and GPS time series. The agreement of the wavelet coefficients time series of the InSAR and GPS data suggests that the InSAR data are not dominated by uncorrected atmospheric delay.

Please cite this article in press as: M. Shirzaei et al., Aseismic deformation across the Hilina fault system, Hawaii, revealed by wavelet analysis of InSAR and GPS time series, Earth Planet. Sci. Lett. (2013), http://dx.doi.org/10.1016/j.epsl.2013.06.011

The statistical significance of this hypothesis is tested below. The periods of 0–0.2 years present the highest detectable frequency in our data set (Fig. 4a1). Given the ~60 days sampling of SAR data, this frequency band is most likely representing the observation noise. The next investigated class spans periods of 0.2–0.5 years (Fig. 4b1). The plot of the amplitude of the global wavelet spectrum associated with this class is characterized by two zones of high amplitude in the southeast and southwest. We find that both of them are clearly bounded by known fault segments of the HFS (the Holei Pali and western Hilina Pali). The zones to the west and east are also identified by the cluster analysis (see Fig. 3). In the class of periods of 0.5–1.0 years the signal over the south-western block is still characterized by large values (Fig. 4c1). At periods of 1.0–1.5 and 1.5–2.0 years (Figs. 4d1–4e1), we find some zones along the HFS that experience larger values. The last class, with periods of 2–3 years, shows a very smooth distribution across Kilauea's south flank. Similar results are obtained by analysis of the independent InSAR data set; i.e., fromtrack 429, as shown in the supplementary material (Fig. S7). Note the similarity between the results of signal classification using the wavelet multiresolution and cluster analysis. Despite a fundamental difference between wavelet decomposition and cluster analysis, in that the former explores the frequency content while the latter compares the amplitude of the signal, both approaches yield comparable results.

4.2. Statistical significance of the similarity between InSAR and GPS

In the previous section, we showed that the wavelet classification of the InSAR time series yields several distinct classes coinciding with HFS-bounded blocks, which are in a good agreement with results obtained by the cluster analysis. Moreover, the comparison of the wavelet coefficients of the InSAR and GPS data analysis (Figs. 4a2–4f6) shows good agreement between corresponding wavelet coefficients. Here, we investigate the statistical significance of these results using Eq. (7). This statistical test allows for examining the similarity between wavelet components of the InSAR and GPS time series. Here, we assume that the variance–covariance matrix of the InSAR and LOS projection of GPS observations is diagonal with standard deviation of 5 and 3 mm, respectively. We also assume that the GPS data are atmospheric-delay free. Thus, if the wavelet-coefficients-difference falls in the range obtained from Eq. (7), it means that the components of the InSAR time series are not distorted by atmospheric delay and that the classes obtained following cluster analysis and wavelet decomposition indicate differential motion at HFS. The results of this analysis are shown in Fig. 5. The upper and lower bounds of Eq. (7) are calculated at 95% confidence level and are shown in red while the wavelet-coefficients-difference associated with the GPS time series and InSAR data near the GPS stations are provided in black. We find that the wavelet-coefficients-difference for the class of periods of 0.0–0.2 years are close to the bound obtained by the statistics, thus they likely reflect observation noise. However, for most of the coefficients in the longer-period classes the test passes, namely, the wavelet-coefficients-difference is in the acceptable range according to the observation noise. Thus, this test shows that at 95% confidence level the atmospheric delay affecting InSAR data is negligible. This result supports the significance of transient or episodic activity along the HFS, especially at periods of 0.2–0.5 years. Moreover, as seen in Figs. 2–4, the identified classes are sharply bound by the high scarps of the HFS, which present the surface expression of the fault segments. The lines of evidence we developed in this section allow for the interpretation that the activity is related to time-dependent faulting along the HFS.

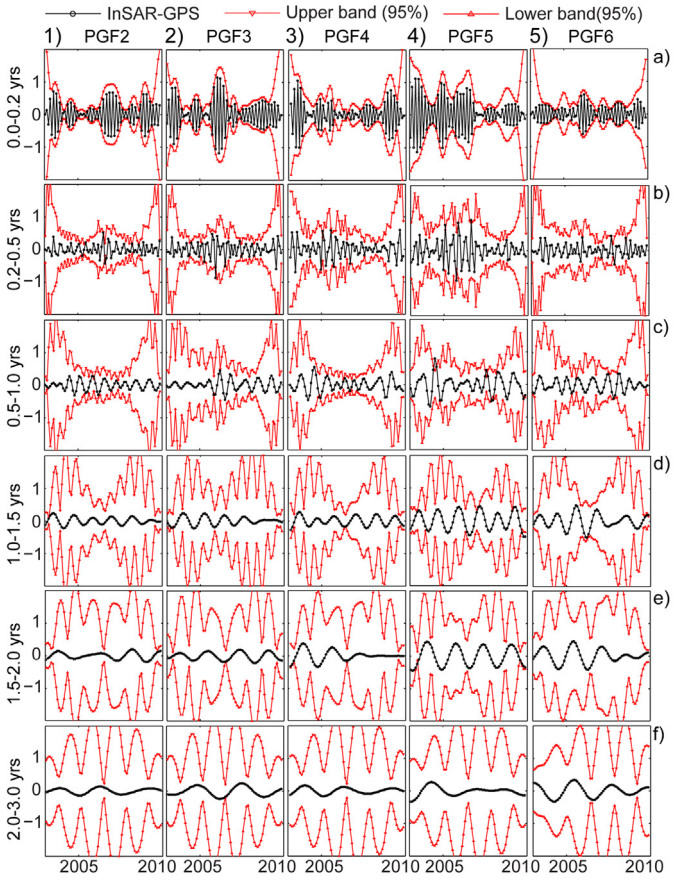

Fig. 5. The statistical significance of the wavelet-coefficients-difference of InSAR and GPS deformation time series. If the wavelet-coefficients-difference (black line) falls in the range obtained from the statistical test in Eq. (7) (red line) then the InSAR data are inferred to not be affected by systematic errors.

5. Discussion

We consider the spatiotemporal surface deformation along the HFS on Kilauea's south flank that is obtained from interferometric analysis of two independent SAR datasets as well as continuous GPS observations. Based on evidence obtained from individual wrapped interferograms, cluster analysis and wavelet decomposition of the InSAR and GPS time series data, we suggest that there is time-variable differential deformation across the HFS. We support this hypothesis by a statistical test built upon the wavelet multiresolution analysis and conclude that at 95% confidence level the deformation classification at HFS is not due to artefacts from atmospheric delay.

The movements are bounded by sharp topography gradients associated with high fault scarps of the HFS, thus the detected signal may represent active block-wise movement. Due to the sparse distribution of the GPS stations near the HFS, this block-wise movement was not detectable before. We also do not find net offset across the HFS in the LOS velocity maps of the InSAR data (Figs. 1a and S2b), possibly due to low rate of deformation overprinted by large seaward motion of the whole south flank and due to repeated reversal of the movement (Fig. S5). However, the wavelet analysis of the high-resolution InSAR data allows for the identification of low-amplitude signals that are hidden due to superposition of other components with large amplitude and their complex temporal behavior. Therefore, this study presents a clear example of the complementary nature of the high spatial resolution InSAR data and GPS time series at a small number of points.

In Fig. 6 the differential time series of displacement are shown for the pairs of panels spanning the western Hilina and eastern

Please cite this article in press as: M. Shirzaei et al., Aseismic deformation across the Hilina fault system, Hawaii, revealed by wavelet analysis of InSAR and GPS time series, Earth Planet. Sci. Lett. (2013), http://dx.doi.org/10.1016/j.epsl.2013.06.011

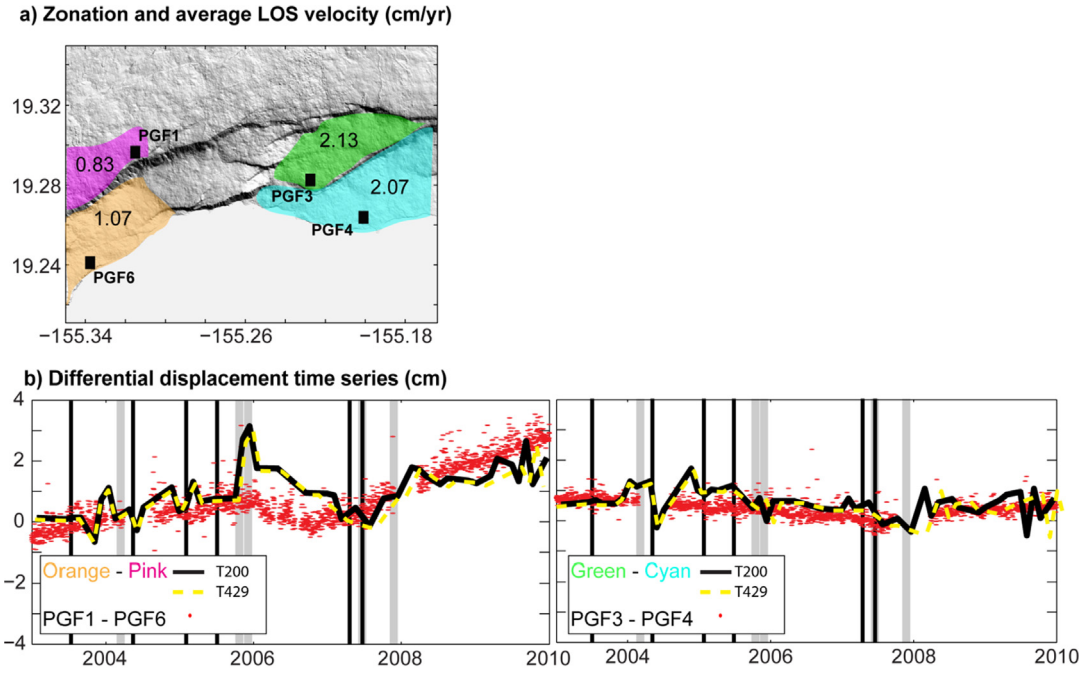

Fig. 6. (a) Colored panels represent relatively coherently moving blocks based on the InSAR deformation over the HFS according to Figs. 2–4 and traces of mapped faults, which are used to compare with GPS data. Each block is labeled by its average LOS velocity. (b) Time series of the differential displacement across the western Hilina Pali (orange relative to magenta panel) and across the Holei Pali (cyan relative to green area), perpendicular to the main HFS fault traces. The solid black lines show the differential LOS time series from track 200 data and red dots are the GPS time series of relative, HFS-normal (Azimuth ∼130°) motion between pairs of stations on the respective blocks. Yellow dashed lines follow the corresponding LOS time series for track 429. Dark grey vertical bars indicate major magmatic activities and the black bars are associated with detachment slip episodes (see Table S1).

Holei Palis. The zones are chosen roughly based on cluster analysis results and trace of major faults. The solid black line shows the differential LOS time series for SAR track 200, the dashed yellow line is the equivalent result for track 429 and red dots are the GPS time series of horizontal motion perpendicular to the trend of the HFS. The names of the GPS stations are provided in Fig. 6. In both panels the InSAR and GPS show similar long term trends, which is likely due to Kilauea inflation through 2006 and the subsequent deflation (Poland et al., 2012). There are several short-term fluctuations in the InSAR differential time series, which sometimes coincide with the timing of several of the marked magmatic events and SSEs (see Table S1). The alternating deformation pattern suggests that the strain regime switches from contraction to extension and vice versa.

An additional factor, which may cause differential deformation within a zone of heterogeneous stress, is the contrast in the elastic properties of the rocks (Fialko et al., 2002). Though there is no direct evidence for such heterogeneities within the HFS blocks, however, a 50% variation in the shear modulus can cause 5 mm of vertical differential displacement across the blocks of HFS. The ∼50% shear modulus contrast is suggested for fault zones near the 1999 Hector Mine earthquake rupture (Fialko et al., 2002) and the normal stress is estimated to be 0.35 MPa as the ratio of variations of the PGF1–PGF6 baseline (∼4 cm) and the N–S distance between stations (∼3 km).

Thus, we may consider a combination of two mechanisms to explain the observed differential deformation across the HFS: (1) slip of weak faults that respond to fluctuations of the strain field allowing them to flip their sign of slip from reverse to normal and vice versa, (2) elastic response of the HFS blocks to changes of the normal stress.

Historically, over fifteen giant landslides occurred around the Hawaii Islands that caused tsunami waves of up to 300 m in the Pacific Ocean (McMurtry et al., 2004; Moore et al., 1994). Damaging local tsunamis also result from more modest incremental sliding associated with M 7–8 earthquakes on Kilauea's basal decollement (Ma et al., 1999; Owen and Burgmann, 2006). These landslides, though infrequent, have the potential for causing huge loss of life and property and it is important to study and investigate the possible mechanisms that may enhance their occurrence. The relation between rift dike intrusions and slip on the basal decollement is well understood (Brooks et al., 2008; Montgomery-Brown et al., 2010), and this study shows that the major blocks bounded by the HFS are also not stable but rather move aseismically in response to subtle changes in the deformation across Kilauea's south flank.

6. Conclusions

The steady seaward motion of Kilauea's south flank is intermittently accelerated by seismic and silent slip events on its basal decollement. However, since the last great earthquakes, there has been no geodetic or seismic evidence for recent activity on the normal faults of the HFS, which represent the head scarps of a large-scale landslide complex on the south flank. This study presents the first evidence of block-wise deformation of the HFS in the absence of major seismicity. The detection of this aseismic deformation improves our understanding of the faulting process on the HFS and highlights the importance of densifying geodetic monitoring networks across the HFS to better monitor, model and interpret this process.

Acknowledgements

Thanks to Mike Poland for providing the high-resolution digital elevation model and for valuable discussions. The interferograms used in this study were generated using the GMTSAR software (Sandwell et al., 2011). Radar data were provided by the European Space Agency under project C1P-9539. The Kılauea and Mauna Loa GPS networks are supported by grants from the USGS, NSF, and

NASA and operated in collaboration by the USGS, Stanford University and the Pacific GPS Facility at the University of Hawaii.

Appendix A. Supplementary material

Supplementary material related to this article can be found online at http://dx.doi.org/10.1016/j.epsl.2013.06.011.

References

Ando, M., 1979. The Hawaii earthquake of November 29, 1975: Low dip angle faulting due to forceful injection of magma. J. Geophys. Res. 84 (13), 7616–7626.

Brooks, B.A., Foster, J.H., Bevis, M., Frazer, L.N., Wolfe, C.J., Behn, M., 2006. Periodic slow earthquakes on the flank of Kīlauea volcano, Hawaii. Earth Planet. Sci. Lett. 246, 207–216.

Brooks, B.A., Foster, J., Sandwell, D., Wolfe, C.J., Okubo, P., Poland, M., Myer, D., 2008. Magmatically triggered slow slip at Kilauea volcano, Hawaii. Science 321 (5893), 1177.

Cannon, E., Bürgmann, R., 2001. Prehistoric fault offsets of the Hilina fault system, south flank of Kilauea volcano, Hawaii. J. Geophys. Res. 106, 4207–4219.

Costantini, M., Rosen, P.A., 1999. A generalized phase unwrapping approach for sparse data. In: Proceedings of the IEEE 1999 International Geoscience and Remote Sensing Symposium, IGARSS, Hamburg, pp. 267–269.

Everitt, B., 2011. Cluster Analysis. Wiley, London, UK.

Fialko, Y., Sandwell, D., Agnew, D., Simons, M., Shearer, P., Minster, B., 2002. Deformation on nearby faults induced by the 1999 Hector Mine earthquake. Science 297 (5588), 1858–1862.

Franceschetti, G., Lanari, R., 1999. Synthetic Aperture Radar Processing. CRC Press.

Goff, J., Dudley, W.C., deMaintenon, M.J., Cain, G., Coney, J.P., 2006. The largest local tsunami in 20th century Hawaii. Mar. Geol. 226, 65–79.

Herring, T.A., 2005. GLOBK, Global Kalman filter VLBI and GPS analysis program. Version 10.2, Release 10.2. Mass. Instit. of Tech.

Hetland, E.A., Muse, P., Simons, M., Lin, Y.N., Agram, P.S., DiCaprio, C.J., 2012. Multiscale InSAR Time Series (MInTS) analysis of surface deformation. J. Geophys. Res.: Solid Earth 117.

Houser, C., Masters, G., Shearer, P., Laske, G., 2008. Shear and compressional velocity models of the mantle from cluster analysis of long-period waveforms. Geophys. J. Int. 174 (1), 195–212.

King, R.W., Bock, Y., 2005. Documentation for the GAMIT GPS Analysis software. Release 10.2. Mass. Instit. of Tech., Scripps Inst. Oceanogr.

Lekic, V., Cottaar, S., Dziewonski, A., Romanowicz, B., 2012. Cluster analysis of global lower mantle tomography: A new class of structure and implications for chemical heterogeneity. Earth Planet. Sci. Lett. 357, 68–77.

Luhr, J.F., Navarro-Ochoa, C., Savov, I.P., 2010. Tephrochronology, petrology and geochemistry of Late-Holocene pyroclastic deposits from Volcan de Colima, Mexico. J. Volcanol. Geotherm. Res. 197 (1–4), 1–32.

Ma, K.F., Kanamori, H., Satake, K., 1999. Mechanism of the 1975 Kalapana, Hawaii, earthquake inferred from tsunami data. J. Geophys. Res.: Solid Earth 104 (B6), 13153–13167.

McMurtry, G.M., Watts, P., Fryer, G.J., Smith, J.R., Imamura, F., 2004. Giant landslides, mega-tsunamis, and paleo-sea level in the Hawaiian Islands. Mar. Geol. 203 (3–4), 219–233.

Montgomery-Brown, E.K., Sinnett, D., Poland, M., Segall, P., Orr, T., Zebker, H., Miklius, A., 2010. Geodetic evidence for en echelon dike emplacement and concurrent slow slip during the June 2007 intrusion and eruption at Kīlauea volcano, Hawaii. J. Geophys. Res. 115, B07405, http://dx.doi.org/10.1029/2009JB006658.

Moore, J.G., Normark, W.R., Holcomb, R.T., 1994. Giant Hawaiian underwater landslides. Science 264 (5155), 46–47.

Morgan, J.K., Moore, G.F., Clague, D.A., 2003. Slope failure and volcanic spreading along the submarine south flank of Kilauea volcano, Hawaii. J. Geophys. Res. 108 (B9), 2415.

Owen, S.E., Burgmann, R., 2006. An increment of volcano collapse: Kinematics of the 1975 Kalapana, Hawaii, earthquake. J. Volcanol. Geotherm. Res. 150 (1–3), 163–185.

Parfitt, E.A., Peacock, D.C.P., 2001. Faulting in the South Flank of Kilauea volcano, Hawaii. J. Volcanol. Geotherm. Res. 106 (3–4), 265–284.

Poland, M.P., Miklius, A., Sutton, A.J., Thornber, C.R., 2012. A mantle-driven surge in magma supply to Kīlauea volcano during 2003–2007. Nat. Geosci. 5, 295–300.

Sandwell, D., Mellors, R., Tong, X., Wei, M., Wessel, P., 2011. Open radar interferometry software for mapping surface deformation. Eos Trans. AGU 92 (28), http://dx.doi.org/10.1029/2011EO280002.

Shirzaei, M., 2013. A wavelet-based multitemporal DInSAR Algorithm for monitoring ground surface motion. IEEE Geosci. Remote Sens. Lett. 10 (3), 456–460.

Shirzaei, M., Bürgmann, R., 2012. Topography correlated atmospheric delay correction in radar interferometry using wavelet transforms. Geophys. Res. Lett. 39 (1), http://dx.doi.org/10.1029/2011GL049971.

Shirzaei, M., Walter, T.R., 2011. Estimating the effect of satellite orbital error using wavelet-based robust regression applied to InSAR deformation data. IEEE Trans. Geosci. Remote Sens. 49 (11), 4600–4605.

Simpson, R.W., Thatcher, W., Savage, J.C., 2012. Using cluster analysis to organize and explore regional GPS velocities. Geophys. Res. Lett. 39.

Tibshirani, R., Walther, G., Hastie, T., 2001. Estimating the number of clusters in a data set via the gap statistic. J. R. Stat. Soc., Ser. B Stat. Methodol. 63, 411–423.

Torrence, C., Compo, G.P., 1998. A practical guide to wavelet analysis. Bull. Amer. Meteor. Soc. 79, 61–78.

Please cite this article in press as: M. Shirzaei et al., Aseismic deformation across the Hilina fault system, Hawaii, revealed by wavelet analysis of InSAR and GPS time series, Earth Planet. Sci. Lett. (2013), http://dx.doi.org/10.1016/j.epsl.2013.06.011